

# Effect of the Transmission Number on Image Quality in Synthetic Aperture Imaging

Riccardo Madonia<sup>1</sup>, Johanne Niman Abildgaard<sup>1</sup>

## ABSTRACT

Synthetic Aperture (SA) imaging enhances ultrasound resolution by emulating a large aperture through sequential transmissions and coherent reconstruction. This study evaluates how the number of transmissions influences image quality, using Field II simulations and in-vitro experiments with a linear array transducer. Point targets and cyst phantoms were assessed for lateral resolution, contrast ratio (CR), and contrast-to-noise ratio (CNR). Lateral resolution degraded with depth, showing a 23.4% increase in FWHM between 10 and 50 mm. CR improved with more transmissions, with the largest gain from 33 to 65, while additional frames provided limited benefit. CNR, however, continued to increase with all transmissions due to speckle averaging, particularly for cysts at greater depths.

Both simulated and experimental results confirmed that using every second transmission (65) offers an optimal balance, retaining most contrast gains while reducing computational demands, thus demonstrating the effectiveness of SA imaging for improving resolution and contrast.

## INTRODUCTION

Synthetic Aperture (SA) imaging is a beamforming technique used in ultrasound to improve the resolution of 2D brightness-mode (B-mode) acquisitions by coherently combining low-resolution images (LRI) acquired from the back-scattered signal.

In conventional B-mode imaging, lateral resolution is limited by the physical aperture size of the transducer which affects the beamwidth.

Unlike the conventional beamforming technique, where a physically larger aperture size is required for narrower beams and higher lateral resolution, SA imaging emulates a large effective aperture by sequentially transmitting from different locations and computationally reconstructing the image.

This study investigates how the number of transmissions affect the quality of the image reconstructed by simulating the SA beamforming process. Specifically, the Field II program is used in MATLAB for simulating a linear array transducer to generate raw Radio Frequency (RF) data for both point targets and a phantom cyst. The contrast resolution (CR) will be quantified for the first case as a primary quality metric, while the contrast-to-noise ratio (CNR) will be assessed for the cyst case. The results are

eventually compared with RF data collected from an in-vitro experiment for both cases.

## METHODS

**Transducer Setup.** An ultrasound transducer generally consists of an array of piezoelectric elements that vibrate when excited by an electrical pulse, producing ultrasound waves that propagate into the medium. These elements then detect echoes from point scatters in the form of RF signals, which are processed to form the LRIs.

In this work, a 192-element linear array transducer was modeled with a center frequency of  $f_0 = 7 \text{ MHz}$  and sampling rate of  $f_s = 100 \text{ MHz}$ , ensuring fulfilment of the Nyquist theorem to allow for proper signal reconstruction. The physical dimensions of each element (0.2 mm width x 5 mm height) and the elevation focus (30 mm) were used in the simulation to define the transmit and receiver aperture for the scanning. Moreover, an inter-element gap  $\text{kerf} = 0.03 \text{ mm}$  was considered to design the array pitch (width + kerf) [Table 1].

Only 64 elements of the transducer were set active for transmission, whereas the whole array was activated for the receiving phase. The

transmit sequence parameters included a transmitter  $F_{tx}\# = -1$ , a receiver  $F_{rx}\# = 1$ , and a total of 129 transmissions with virtual sources pitch-spaced (pitched array) [Table 2].

**Table 1.** Linear array setup properties

Parameter	Value	Unit
elements number	192	
element height	5	mm
element width	0.2	mm
kerf	0.03	mm
elevation focus	30	mm
transducer center frequency	7	MHz
transducer sampling rate	100	MHz

**Table 2.** Transmit sequence properties

Parameter	Value
transmitting active elements	64
receiving active elements	192
transmit $F_{tx}\#$	-1
receive $F_{rx}\#$	1
number of transmissions	129
virtual sources spacing [mm]	0.23

**Data Simulation.** RF data was simulated by modeling the transducer excitation  $e(t)$  and impulse response  $v(t)$ , carefully matching the transducer characteristics. Specifically, the excitation was defined as a single-cycle sinusoidal wave at the center frequency  $f_0$ ,

$$e(t) = \sin(2\pi f_0 t), \quad 0 \leq t \leq \frac{1}{f_0}$$

while the transducer impulse response to this pulse was defined as a sinusoidal wave oscillating for two complete periods at the center frequency  $f_0$ , then modulated by a Hanning window to limit spectral leakage [Fig.1].

$$v(t) = \sin(2\pi f_0 t) \cdot \text{hann}(t), \quad 0 \leq t \leq \frac{2}{f_0}$$

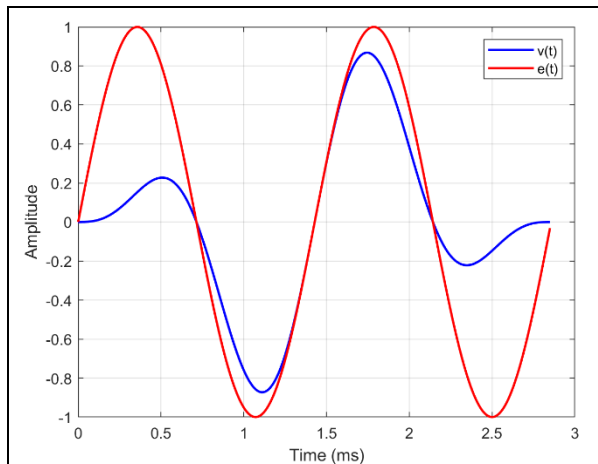


**Figure 1.** Excitation and transducer impulse response in time and frequency domain.

Eventually, a Hamming apodization window was applied to the active transmit elements to reduce sidelobe levels and improve contrast resolution.

To assess the SA beamforming performance, two simulated phantoms were acquired: (1) point targets with five scatterers positioned at depths of 10, 20, 30, 40, and 50 mm, and (2) a cyst of 3 mm radius at a 30 mm depth, containing 10,000 scatterers. Additive white noise was applied to the raw RF data for the phantom cyst to mimic electronic noise before the beamforming process.

Data acquisition was performed over 129 transmissions, each corresponding to a unique transmit event where the 64 active elements generated a wavefield. Therefore, the width of the image was determined by the number of transmissions, with the first one placed at the leftmost virtual source location.

For each transmission, the virtual source was set behind the array to simulate the negative focal ratio ( $F_{tx}\# = -1$ ), and its lateral position was sequentially incremented by the pitch to steer the beam across the imaging field.

A dynamic Hamming apodization window was applied to shape the excitation contribution of a contiguous block of 64 elements, with the active transmit aperture shifting laterally along the array. The scattering response from the phantom was simulated using the Field II function *calc\_scatt\_multi*, and the resulting RF data was zero-padded before storage to compensate for variations in delay times.

**SA beamforming.** A low-resolution image was generated from each transmission using a beamforming process implemented in the *imageFormation* function. The image grid was defined with a pixel size of  $0.1 \times 0.1 \text{ mm}^2$ , and, for each pixel, time-of-flight delays were computed based on both the transmit ( $tx_{path}$ ) and receive ( $rx_{path}$ ) path lengths as:

$$ToF_{ij} = \frac{tx_{path} + rx_{path}}{c},$$

where

$$tx_{path} = \sqrt{(x_{VS} - x_{ij})^2 + (z_{VS} - z_{ij})^2} + z_{VS}$$

and

$$rx_{path} = \sqrt{(x_{el} - x_{ij})^2 + (z_{el} - z_{ij})^2}$$

with  $(x_{VS}, z_{VS})$  representing the coordinates of the virtual source ( $VS = 1, 2, \dots, 129$ ),  $(x_{ij}, z_{ij})$  the lateral and depth position of a pixel on the image grid ( $i = 1, 2, \dots, \text{image width}$  and  $j = 1, 2, \dots, \text{image depth}$ ),  $(x_{el}, z_{el})$  the position of the dynamic aperture elements relative to the transducer, and  $c$  the speed of sound in the medium assumed as 1540 m/s.

To maintain a consistent receiver  $F_{rx}\# = 1$ , the function dynamically adjusts the center of each receive aperture on the lateral index of the processed pixel. The number of elements to activate is then determined as a function of the pixel depth according to the *F-number* definition:

$$F\# = \frac{\text{depth}}{\text{aperture width}}$$

Since  $F\# = 1$ , the transducer elements activated were determined directly by the pixel's depth  $z_{ij}$ , scaled by the element pitch to align the aperture with the locations of the transducer elements. The range of active elements was computed symmetrically around the central element, to ensure a balanced aperture. The starting index of the active aperture was calculated by subtracting half of the number of active elements from the center, while the end index was determined by adding same quantity to the center. Any aperture elements exceeding the physical boundaries of the transducer were discarded ensuring that the active aperture remained within the original physical size of the transducer.

$$N_{\text{active}} = \frac{z_{ij}}{F_{rx}\# \cdot \text{pitch}}$$

Before storing the delay results for each pixel, the Hamming apodization window was applied only to the defined aperture, reducing the contribution of off-axis elements and enhancing the lateral resolution. Cubic interpolation was then used to extract the corresponding RF data, and, eventually, the contributions from the active elements, i.e. the LRI of each transmission, were summed up to form the HRI.

**Image Quality Evaluation.** The *full width at half maximum* (FWHM) was quantified at the depth of each of the five points to first assess the lateral resolution of the simulated SA imaging system, meaning its ability to resolve two closely spaced objects. For this evaluation, the lateral intensity profile at the depth of each point target was extracted from the HRI and normalized to a scale between 0 and 1. Linear interpolation was then applied at half of the peak intensity to obtain a

precise estimate of the width at 50% of the maximum signal. This process was enhanced by upsampling the lateral profile to improve the resolution of the measurement.

Experimental data for both point targets and cysts were acquired using a research ultrasound scanner, following the same transmit sequence as the simulation but with a sampling rate of 62.5 MHz. The point targets consisted of thin wires submerged in water at room temperature, which led to a reduction in the speed of sound  $c$  from 1540 m/s to 1480 m/s.

To further evaluate the image quality and investigate the effect of reducing the number of transmissions in the HRI, two contrast metrics were assessed: the *contrast ratio* (CR) for point scatterers and the *contrast-to-noise ratio* (CNR) for cystic regions.

The CR quantifies the extent of distinguishability of the target from its surroundings in the image, and it is generally defined as the ratio of the energy outside a target region to the total energy in a surrounding region [Eq.5]. A higher CR value indicates better contrast resolution and enhanced target visibility against the background.

To compute the CR, a square region of 10x10 mm centered on the target was first selected. Within this square, a circle with a radius of  $r = 2.5\lambda$  was then used to define the point spread function (PSF) region, distinguishing the target from the surrounding sidelobes within the region of interest (ROI). The total energy ( $E_{\text{total}}$ ) within the square ROI and the energy ( $E_{\text{out}}$ ) outside the target region were calculated by summing the squared magnitudes of the pixel intensities within the respective regions. The results were then converted to dB scale for improved analysis.

$$CR = 20 \log_{10} \left( \frac{E_{\text{out}}}{E_{\text{total}}} \right)$$

Similarly, the CNR evaluates how well the contrast of an object, such as a cyst, can be distinguished from background noise in an image. For this evaluation, two square regions of 2x2 mm were selected both within the cyst and within an adjacent tissue region at the same depth. The CNR was then calculated as the ratio between the difference of the mean intensities of the cyst ( $\mu_{\text{cyst}}$ ) and tissue ( $\mu_{\text{tissue}}$ ) to the square root of their squared standard deviations. Again, the results were then converted to dB scale.

$$CNR = 20 \log_{10} \left( \frac{|\mu_{cyst} - \mu_{tissue}|}{\sqrt{\sigma_{cyst}^2 + \sigma_{tissue}^2}} \right)$$

## RESULTS AND DISCUSSION

**Lateral Resolution.** The FWHM value provides the lateral width at which the intensity drops to half of its peak value, effectively measuring the spread of the point spread function (PSF). Therefore, a point target in an image ideally produces a small spot with maximum intensity at its center, providing a narrow FWHM, which reflects a system able to finely distinguish small objects with high resolution. In simulation, the lateral intensity profiles showed a consistent

peak (normalized) at the center, confirming the presence of a well-defined maximum. The main insight, however, lies in the width of these profiles, which increases as the distance from the transducer grows. At 10 mm depth, the system showed its sharpest resolution (0.47 mm), indicating minimal spreading of the beam and precise localization of the point scatterer. As the depth increases, the FWHM worsens, indicating a slight degradation in resolution. At 20 and 30 mm depth, the system lost 0.02 mm, showing a value of 0.49 mm for both cases. This consistent FWHMs suggest the system did not lose quality across this depth range. The resolution slightly worsens further at 40 mm (0.51 mm), until widening at 50 mm depth (0.58 mm) [Fig.2]. This value represents an increase of 0.11 mm compared to the 10 mm measurement.

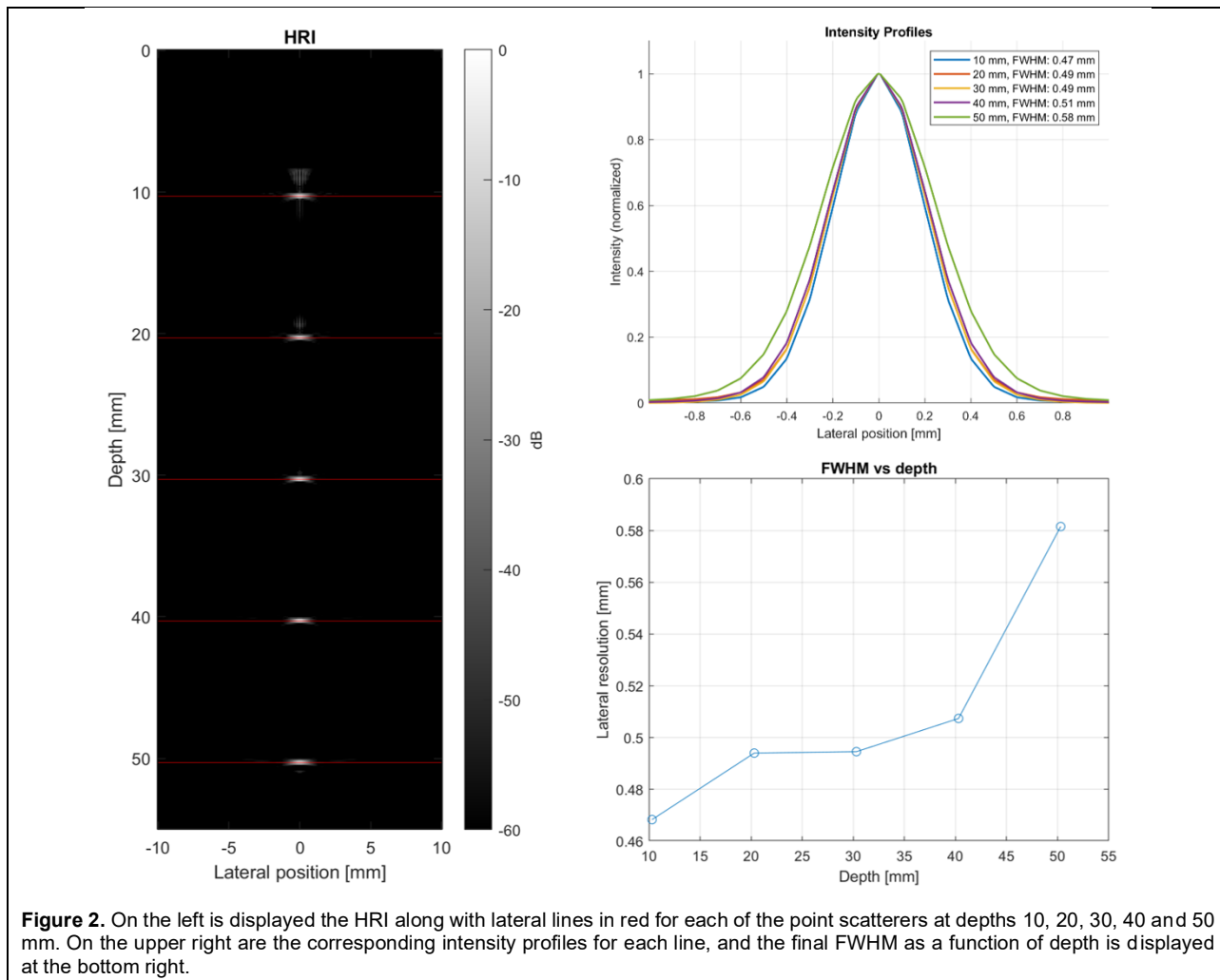


**Figure 2.** On the left is displayed the HRI along with lateral lines in red for each of the point scatterers at depths 10, 20, 30, 40 and 50 mm. On the upper right are the corresponding intensity profiles for each line, and the final FWHM as a function of depth is displayed at the bottom right.

This broadening corresponds to a 23.4% increase in FWHM over the 40 mm depth range, proving a gradual decrease in resolution with increasing depth. This trend is consistent with the expected behavior of ultrasound beams,

where diffraction and optical effects typically cause the beam to spread over distance. Although a 23.4% increase in FWHM might seem significant in some contexts, it suggests a relatively modest loss of resolution over the

measured distances. Whether this change is acceptable depends largely on the specific application's requirements. If the application demands high resolution over large distances, this degradation might be unacceptable. However, if a slight reduction in resolution is tolerable, the system's performance can be considered adequate. To further evaluate the system's performance, additional analysis could be done. For example, examining the beam divergence angle would offer deeper insights into the factors contributing to the observed resolution changes.

**Effect of transmissions number on CR.** The CR was assessed on HRIs formed using different numbers of transmissions for both simulated and in-vitro acquired point targets. By progressively increasing the number of LRIs included in the coherent compounding process, we investigated how the size of the synthesized aperture affects the system's ability to distinguish between targets and background.

A first visualization offered clear qualitative insights into how the brightness of targets improves as more LRIs are coherently summed—from 1 every 10th, 8th, 6th, 4th, 2nd frame, and eventually all 129 frames [Fig.3]. This progression can be directly observed in the images, where sidelobe levels decrease making the main one more pronounced, enhancing target detectability. These figures offer an intuitive understanding of the effect of aperture synthesis on image clarity and contrast resolution.

A quantitative evaluation confirmed this visualization, showing the CR generally increases in magnitude as more LRIs are summed [Fig.4]. According to [Eq.5], this indicates a progressive reduction in sidelobe energy around each point and aligns with the principle that coherent averaging reduces noise and improves signal clarity. The most significant improvement was seen when increasing the summation from every 4th (33) to every 2nd frame (65), where the CR set from  $-12/-15$  dB to its maximum for each point ( $-19$  dB for 10, 20, 30 mm depth,  $-17.5$  dB for 40 mm and  $-14.5$  dB for 50 mm). Conversely, summing up all available LRIs (129) yielded only marginal additional improvement. This suggests that averaging at least half the frames significantly mitigates sidelobe fluctuations while enhancing the main lobe contribution from the target, hence offering an optimal trade-off

between image quality and computational cost.

At lower summation rates, such as 1 every 10th (13) and 1 every 8th frame (17), the CR values exhibited greater variability across target depths (from  $-16$  dB for 30 mm to  $-6$  dB for 50 mm). However, as more frames were included, these values gradually converged, supporting the fact that sufficient averaging diminishes PSF limitations and leads to more uniform image quality.

Targets located at shallower depths exhibit the highest CR values, particularly when the HRI is generated from summing up all frames or at least half of them, suggesting that the synthetic aperture reaches its practical maximum at these depths. This trend is expected, as low-depth targets benefit from a more complete synthetic aperture, which enhances lateral resolution and improves sidelobe suppression. Therefore, the aperture at those depths may not be affected by size reductions due to the physical limit of the transducer, but, for the same reason, the CR decreases for the deepest target (50 mm), where increased attenuation, off-axis scattering, and noise accumulation may also contribute to the contrast degradation, despite the use of all the transducer elements.

Similar results have been observed for the experimental acquisitions [Fig.5]. The CR values leveled off as more frames were included for both targets. As expected, the deeper target at 52 mm showed a lower contrast ratio (around  $-6$  dB) compared to the shallower one at 28 mm (around  $-4$  dB). This trend becomes evident already from choosing 1 every 8th (17) frame in the HRI formation and remains consistent across the subsequent summation strategies. Only a slight improvement was seen after summing up every 4th (33) frame, with the CR values reaching their near-maximum value beyond that point.

When only 1 every 10th (13) frame is summed the resulting image may not fully represent the target's true spatial characteristics. At this stage, the HRI suffers from a higher degree of noise and variability due to the lack of adequate averaging, causing the CR to appear inverted compared to the trend seen with more frames with values of  $-10$  dB for shallower target and  $-2$  dB for deeper one [Fig.6]. Indeed, by considering only 13 LRIs, the synthesis of the aperture is incomplete, leading to poor sidelobe suppression and reduced contrast between the



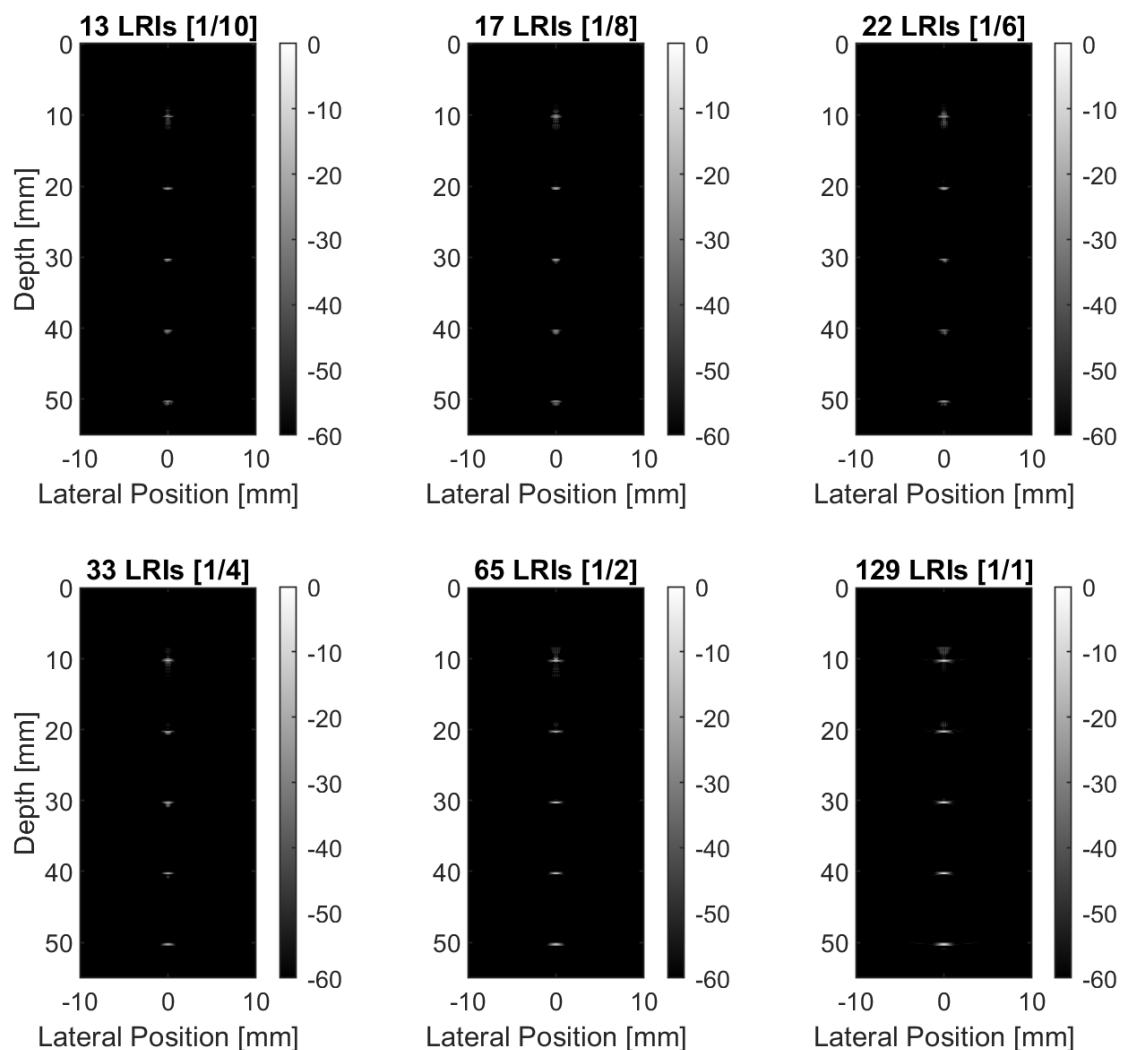


**Figure 3.** On the left is displayed the HRI along with the ROI for the first point target at 10 mm. On the right are the CR values for point targets at depths 10, 20, 30, 40, and 50 mm for different summation strategies, using 13, 17, 22, 33, 65, and 129 transmissions.

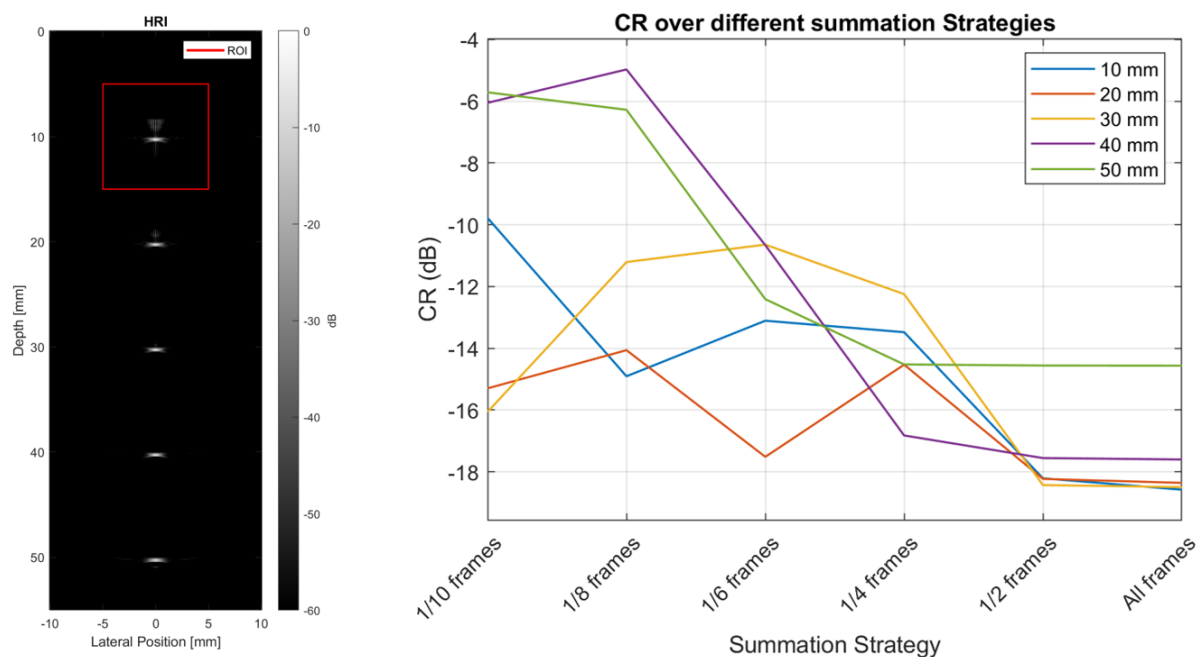


**Figure 4.** On the left is displayed the HRI along with the ROI for the first point target at 10 mm. On the right are the CR values for point targets at depths 10, 20, 30, 40, and 50 mm for different summation strategies, using 13, 17, 22, 33, 65, and 129 transmissions.

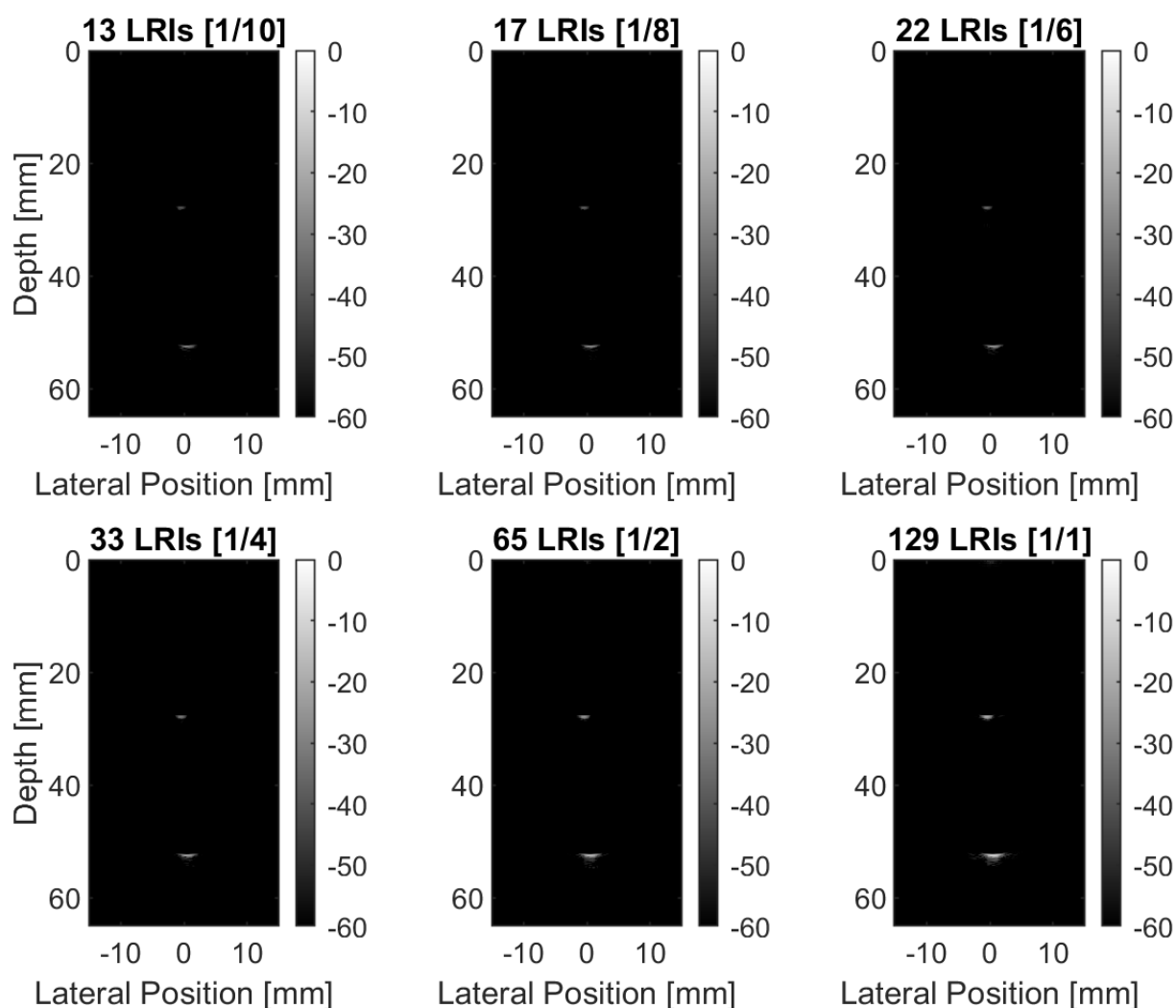


**Figure 5.** Impact of LRIs number on contrast ratio of HRIs of experimental point targets at depths 28 and 52 mm using 13, 17, 22, 33, 65 and 129 transmissions, respectively.

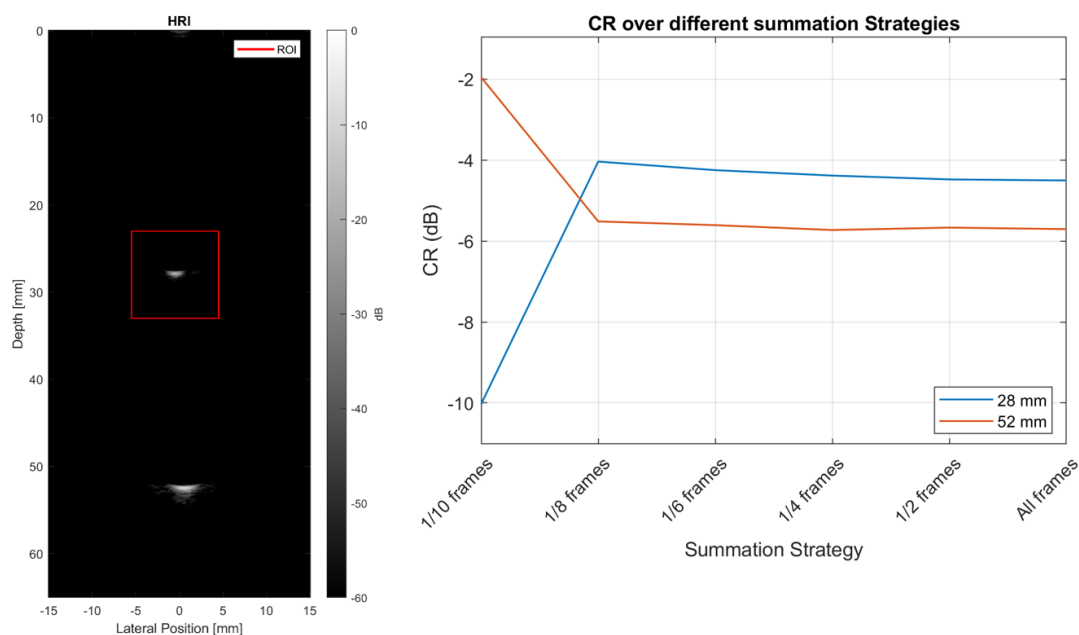
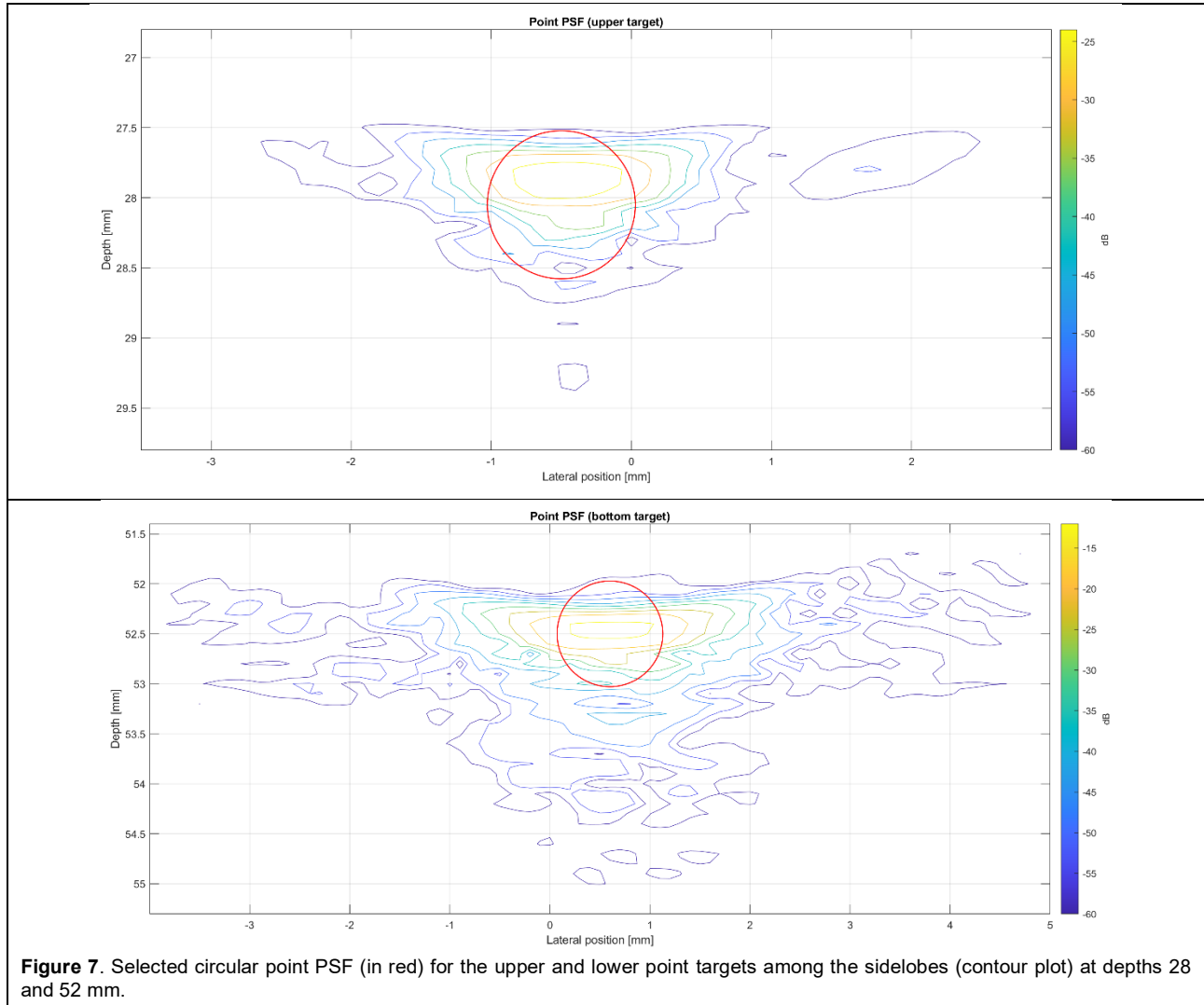


**Figure 6.** On the left is displayed the HRI along with the ROI for the first point target at 28 mm. On the right are the CR for point targets at depths 28 and 52 mm for different summation strategies; using 13, 17, 22, 33, 65 and 129 transmissions, respectively.

target and the background.

Through a visualization of the circular region ( $r = 2.5\lambda \cdot \text{pitch}$ ) used to isolate the point signal from the sidelobes in the fully developed HRI [Fig.7], it can be observed that, even when all 129 LRIs are summed, a significant amount of

sidelobe energy remains outside the selected point spread function (PSF), particularly for the bottom target. This observation accounts for the poor contrast observed in the initial summation strategy.



**Effect of transmissions number on CNR.** The CNR between a water-filled cyst and an adjacent tissue region was similarly assessed on HRIs formed with varying numbers of transmissions [Fig.8]. Similar to the point-target analysis, the number of LRIs included in the coherent compounding process was progressively increased to evaluate how the synthesized aperture influenced the ability to distinguish the cyst from the surrounding tissue. Since CNR primarily depends on the difference in mean intensity between the two ROIs, scaled by the square root of the sum of the standard deviations [Eq.6]) a higher positive value indicates improved contrast, meaning a greater the detectability of the cyst.

The trend observed for the cyst largely mirrored that of the point targets: the CNR increased as more LRIs were summed, with the largest improvement (+2 dB) occurring when the compounding strategy shifted from every 4th frame (−2 dB) to every 2nd frame (0 dB) [Fig.9]. However, unlike point targets, where a plateau in quality was reached beyond that strategy, the cyst exhibits an additional 1 dB improvement when all LRIs were included. This difference can be attributed to the extended spatial nature of the cyst, for which summing more LRIs effectively enhances spatial averaging within both the cyst and the surrounding tissue ROIs.



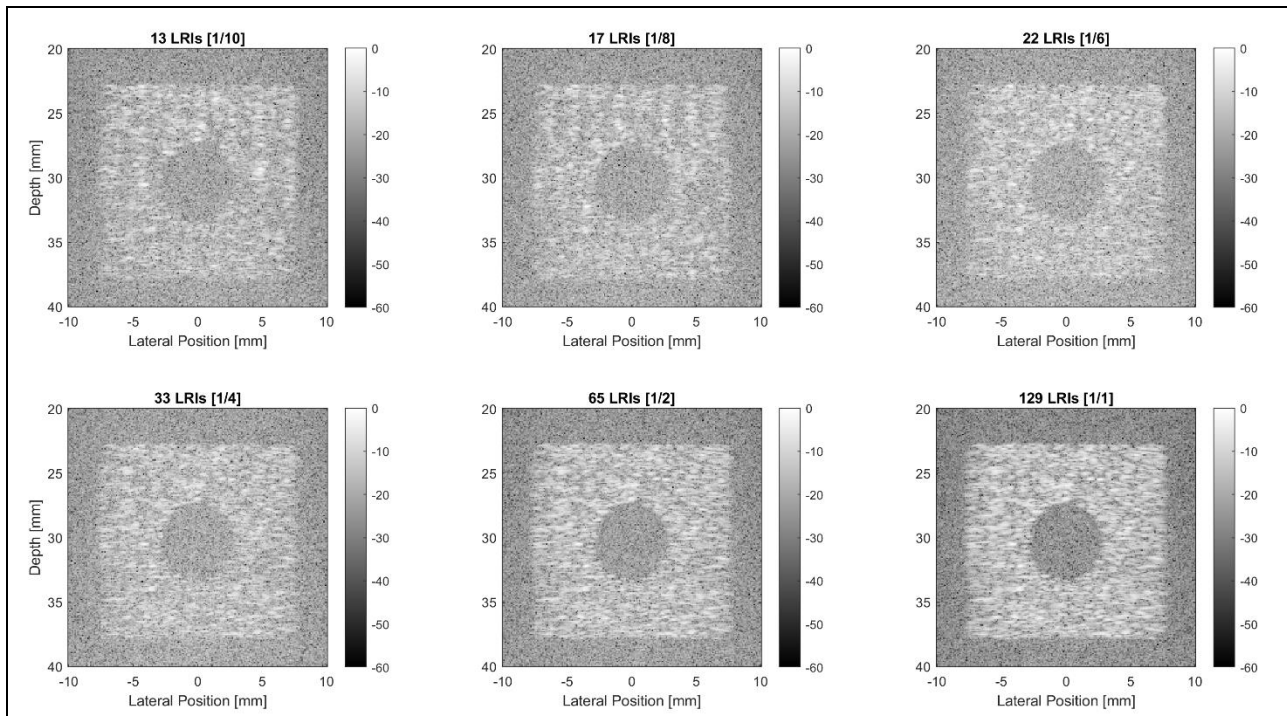


**Figure 8.** Impact of LRIs number on contrast-to-noise ratio of HRIs of simulated cyst phantom using 13, 17, 22, 33, 65 and 129 transmissions, respectively.

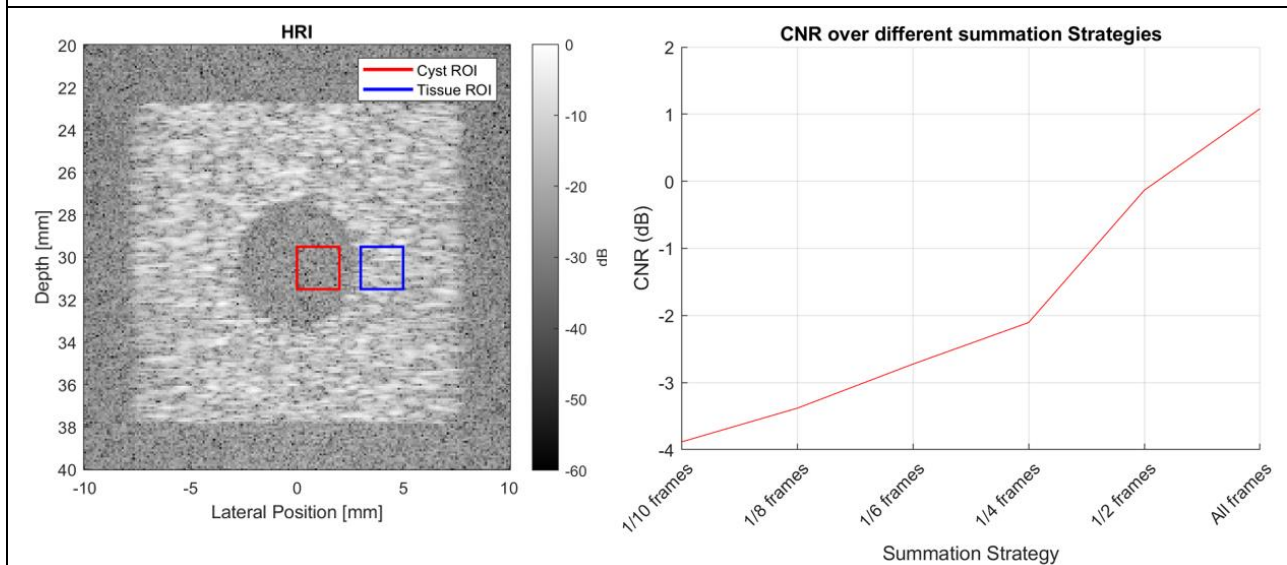


**Figure 9.** On the left is displayed the HRI of the simulated cyst phantom along with the cyst ROI in red and tissue ROI in blue. On the right are the CNR values for different summation strategies, using 13, 17, 22, 33, 65 and 129 transmissions, respectively.

Indeed, averaging reduces the impact of speckle noise, which is a dominant common factor limiting the contrast of extended structures in ultrasound imaging, thereby providing a more accurate and stable estimation of the CNR within each region. Although increased averaging generally benefits CNR by suppressing uncorrelated speckle patterns, trade-offs include a loss in spatial resolution, particularly in the sharpness of the cyst's boundaries. However, in the case observed, the benefits of speckle suppression outweigh any minor blurring effects.

Overall, these findings suggest that for extended structures like cysts, maximizing the number of summed LRIs in coherent compounding can yield significant contrast improvements, potentially enhancing diagnostic confidence. The analysis of the real scanner data generally confirmed the phantom cyst results. The HRI showed both cysts as hypoechoic (darker) regions within a more echogenic (brighter, speckled) surrounding tissue [Fig.10]. Like in simulation, ROIs were placed within each cyst and in a relative adjacent portion of tissue, at the same depth to ensure consistent evaluation.

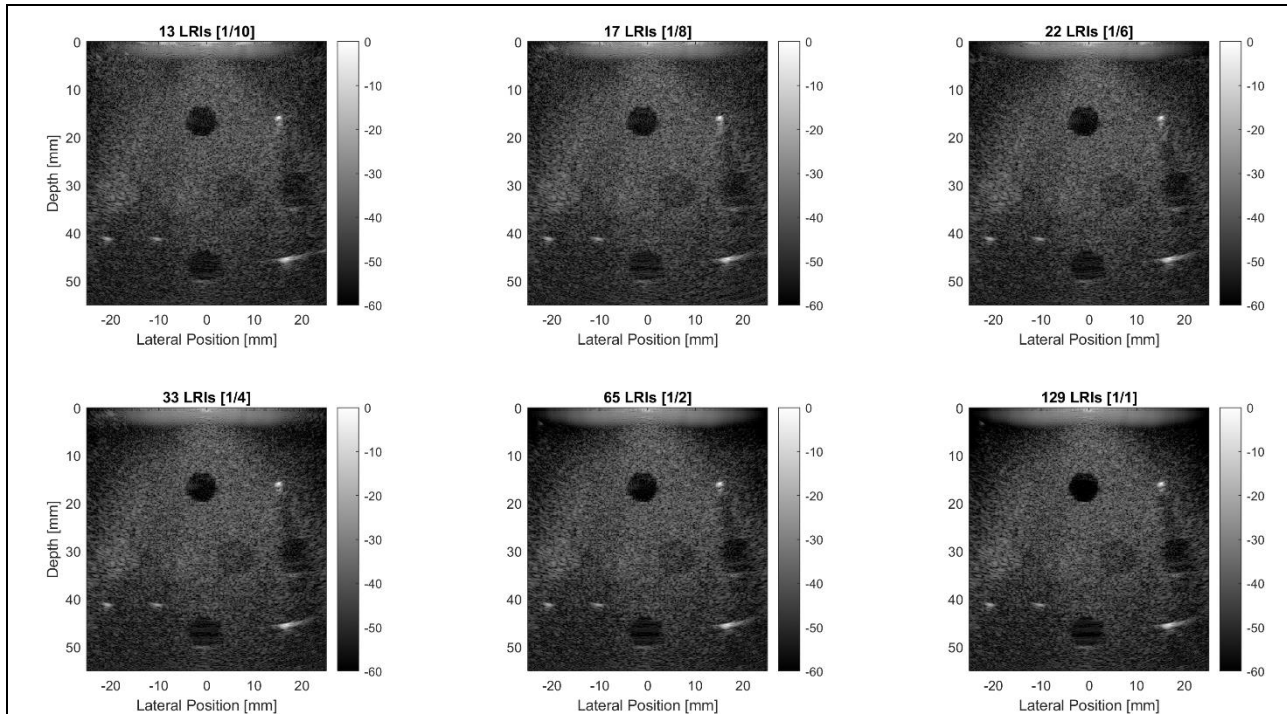


**Figure 10.** Impact of LRIs number on contrast-to-noise ratio of HRIs of experimental cyst phantom using 13, 17, 22, 33, 65 and 129 transmissions, respectively.

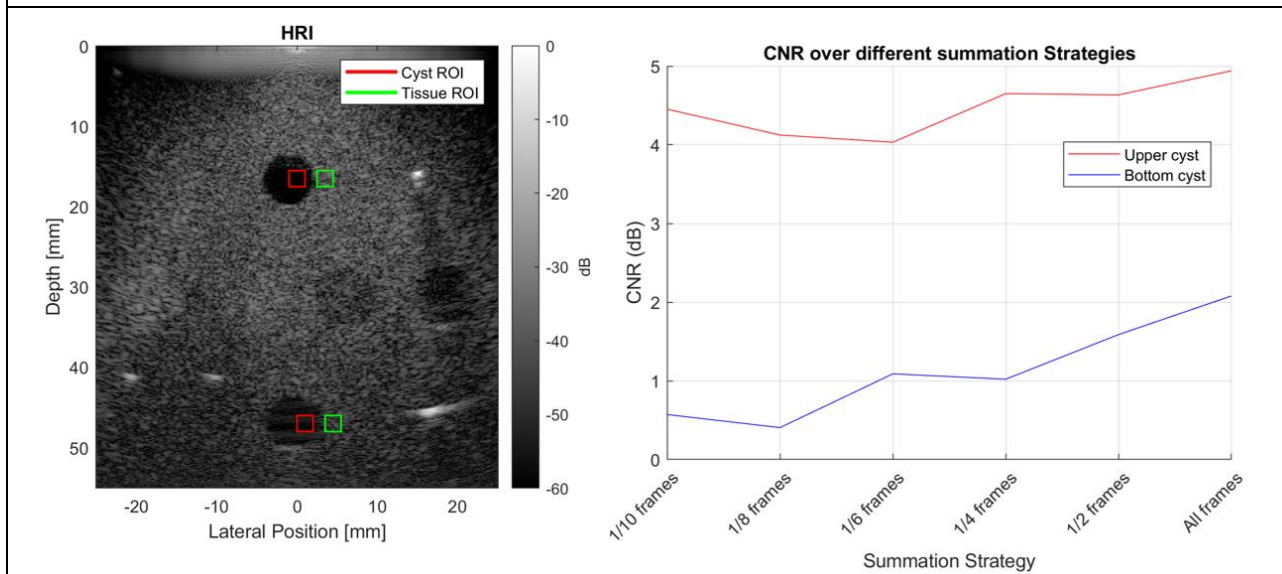


**Figure 11.** On the left is displayed the HRI of the experimental cyst phantom along with the cyst ROIs in red and tissue ROIs in green. On the right are the CNR values for the upper and lower cyst for different summation strategies, using 13, 17, 22, 33, 65 and 129 transmissions, respectively.

For the shallower and deeper cysts, the CNR increased from 4.5 dB to 5 dB and from 0.5 to 2 dB, respectively, as more LRIs were summed. For the upper cyst, the CNR generally showed a trend of improvement with additional frames, a slight drop (0.5 dB) occurred between the 1/8th- and 1/6th-frame strategies. On the other hand, the CNR for the deeper cyst exhibited a more pronounced and consistent increase with increasing numbers of LRIs. As expected, while its initial contrast was lower due to its depth, each compounding increment led to a more

substantial gain [Fig.11]. This suggested that the coherent compounding process was particularly effective for the deeper cyst, likely due to a more significant reduction in noise and speckle interference in its surrounding environment as more data was averaged. Despite these individual variations, both cysts benefitted from increasing the number of summed frames, supporting the results from the phantom study.

## CONCLUSION

Based on the analysis of SA beamforming for both simulated and experimental data, several key findings have been observed regarding the impact of numbers of transmissions on image quality and contrast.

The FWHM measurements displayed a gradual decrease of lateral resolution with increasing depth, with a 23.4% increase in FWHM over the 40 mm depth range. This confirms the expected behavior of ultrasound beam spreading with distance.

It was observed that the CR for point targets generally improves with increasing number of transmissions for both simulated and in-vitro data. The most significant improvement occurs when increasing from 33 to 65 transmissions, with minimal additional benefits from using all 129 transmissions. It was also seen that shallow targets consistently showed better contrast than deeper ones.

CNR for cysts was also seen to improve with more transmissions and showed a continued improvement even when using all available transmissions.

Overall, the results suggest that for most applications, using every 2nd transmission (65) provides a good balance between image quality and computational efficiency. This approach captures most of the available contrast improvements while reducing processing requirements by nearly half.

Both simulated and experimental results confirm that image quality metrics (lateral resolution, CR and CNR) degrade with increasing depth, reflecting fundamental physical limitations of ultrasound propagation. These findings demonstrate the effectiveness of SA imaging for improving resolution and contrast.

## References

- [1] Jensen, J. A. (1996). *Field: A program for simulating ultrasound systems*. Medical & Biological Engineering & Computing, 34, 351–353.
- [2] Jensen, J. A., & Svendsen, N. B. (1992). *Calculation of pressure fields from arbitrarily shaped, apodized, and excited ultrasound transducers*. IEEE Transactions on Ultrasonics, Ferroelectrics, and Frequency Control, 39, 262–267.
- [3] Smith, S. W. (1997). *The Scientist and Engineer's Guide to Digital Signal Processing*. Chapters on beamforming.

- [4] Van der Steen, A. F. W., & van der Kaa, C. A. (1992). *Synthetic aperture imaging in medical ultrasound*. Ultrasound in Medicine & Biology, 18, 407–420.
- [5] Yao, L., & O'Donnell, M. (2002). *Analysis of contrast-to-noise ratio in ultrasound imaging*. Ultrasound in Medicine & Biology, 28, 1033–1040.
- [6] Kim, Y., & Kim, C. (2007). *Comparison of simulated and experimental synthetic aperture ultrasound imaging*. Ultrasound in Medicine & Biology, 33, 1155–1164.